Dynamical Mechanism of the Summer Circulation Trend Pattern and Surface High Temperature Anomalies over the Russian Far East

DONG WAN KIM[a] AND SUKYOUNG LEE[a]

[a] *Department of Meteorology and Atmospheric Science, The Pennsylvania State University, University Park, Pennsylvania*

(Manuscript received 12 April 2022, in final form 8 July 2022)

ABSTRACT: This study investigates the mechanism behind the recent boreal summer circulation trend pattern and associated high surface temperature anomalies over the Russian Far East. This circulation pattern includes a prominent anticyclone over the Kamchatka Peninsula where heat extremes have been trending upward. Observational analysis and numerical model simulations indicate that latent heating anomalies centered over Yakutia, west of Kamchatka Peninsula, can excite this anticyclone and the downstream circulation trend pattern. However, this anticyclone alone is insufficient for generating the anomalously high temperature over the region. Instead, the high temperature emerges when there is an upstream precursor that resembles the Eurasian circulation trend pattern. Warm advection by this upstream circulation initiates a positive temperature anomaly over the Russian Far East, one week prior to the onset of the anticyclone in this region. As this anticyclone develops, the temperature anomalies further intensify by adiabatic warming and shortwave radiative heating. If upstream circulation anomalies are opposite to those of the Eurasian trend pattern, the initial temperature over the Russian Far East is anomalously negative. As a result, the adiabatic warming and shortwave radiative heating within this anticyclonic region are unable to bring the temperature to an extreme condition. These findings indicate that the temperature extremes over the Russian Far East are contributed by a combination of remote and local circulation forcings and provide insights into subseasonal forecasts of heat waves over this region.

KEYWORDS: Atmospheric circulation; Teleconnections; Surface temperature

1. Introduction

The boreal summer circulation trend pattern is known to be associated with a trend in strong surface heat waves (M. Lee et al. 2017). This summer circulation trend pattern, which is the linear trend of the 300-hPa zonal mean removed streamfunction (Fig. 1), consists of an anomalous upper-level anticyclonic circulation trend over Greenland, Europe, central Asia, and the Russian Far East. Each of these regions also exhibits an increase in the frequency of surface heat waves. Understanding the dynamics of the processes that excite this circulation trend pattern on its intrinsic intraseasonal time scale will therefore provide insight into the mechanisms that drive the development of the corresponding high surface temperature anomalies. Previous studies have examined the dynamics of the circulation trend pattern over the Western Hemisphere (Kim and Lee 2021) and Europe and central Asia (Kim and Lee 2022). However, the intraseasonal mechanism responsible for the development of the summer circulation trend pattern over the Russian Far East and the North Pacific (REP; green box in Fig. 1), which includes a prominent anticyclonic trend centered near the Kamchatka Peninsula and a corresponding surface temperature anomaly, remains to be examined. We are further motivated to examine the dynamics of the REP trend pattern because a high-latitude upper level anticyclone has been linked to wildfires (Yasunari et al. 2021), and an anticyclonic blocking-like circulation over the Russian Far East may impact East Asian extreme weather (Yeh et al. 2018).

While the REP trend pattern can be viewed as arising from downstream development of the Eurasian trend pattern (in this study, Eurasia excludes the Russian Far East), earlier studies do not show a clear linkage between Eurasian wave trains and the anomalies that comprise the REP trend pattern (Yasui and Watanabe 2010; Schubert et al. 2014; Kim and Lee 2022), as those Eurasian waves typically propagate following the Asian jet (Hoskins and Ambrizzi 1993; Branstator 2002; Enomoto et al. 2003). Instead, the REP trend pattern could be driven by upstream anomalous diabatic heating, because extratropical diabatic heating (Hoskins and Karoly 1981), especially latent heating anomalies (Pfahl et al. 2015; Steinfeld and Pfahl 2019), are known to excite an upper-level anticyclone and a downstream wave train. Indeed, some of the circulation anomalies that make up the summer circulation trend pattern have been shown to be excited by upstream latent heating anomalies (Baggett and Lee 2019; Kim and Lee 2021, 2022). Therefore, latent heating anomalies can play an important role in generating the REP trend pattern and the corresponding positive temperature anomalies.

The Eurasian circulation trend pattern, however, could still have an impact on surface temperature anomalies over land in the REP domain (red-lined boxes in Figs. 2d–f). Kim and Lee (2022) showed that the Eurasian trend pattern was accompanied by positive surface temperature anomalies over Russian Far East land areas while there was no strong circulation signal over this region. One possible way for significant positive temperature anomalies to arise in association with the REP trend pattern is that positive temperature anomalies are first established by a remote influence of the Eurasian trend pattern as a precondition, and the REP trend pattern could then further amplify the strength and persistence of the

Corresponding author: Dong Wan Kim, dxk582@psu.edu

DOI: 10.1175/JCLI-D-22-0244.1

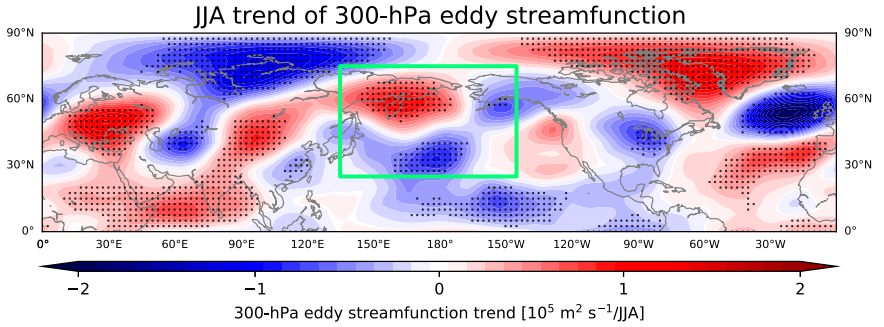

FIG. 1. Linear trend of the June, July, and August mean eddy streamfunction at the 300-hPa level. The trend is computed for the period of 1979–2017 [modified after Kim and Lee (2022)]. Dots represent a statistically significant trend at the 90% level, computed by the Mann–Kendall trend test (Wilks 2011). The green-lined box represents the projection domain of the Russian Far East trend index (see section 2b for details).

warm temperature anomalies. Therefore, the strength of the temperature anomaly associated with the REP trend pattern may be dependent on the presence of the upstream Eurasian circulation pattern.

The goal of this study is thus to explore this possibility by dividing the REP trend pattern events into two groups—those preceded by the Eurasian trend pattern and those preceded by the pattern that opposes the Eurasian trend pattern—and contrasting these two groups using diagnostic analyses and numerical model experiments. The data and methods used in this study are described in section 2, and the results are presented in section 3. Conclusions and discussion follow in section 4.

2. Data and method

a. Data

We used daily mean 300-hPa streamfunction from the ERA-Interim reanalysis (Dee et al. 2011), for the time period of June, July, and August (JJA) from 1979 to 2017. We also used data at the lowest model level of this reanalysis to diagnose the temperature anomaly development over the Russian

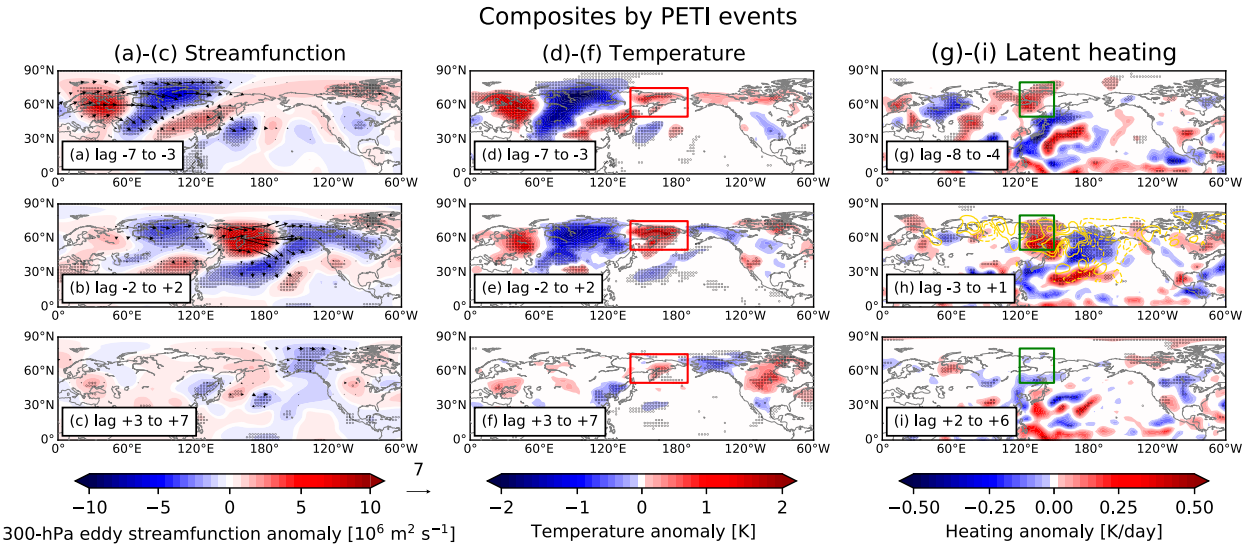

FIG. 2. Pentad composites of the (left) 300-hPa eddy streamfunction anomaly, (center) temperature anomaly at the lowest level of the eta coordinate, and (right) latent heating anomaly during PETI events. Streamfunction and temperature pentads are centered at lag days (a),(d) −5, (b),(e) 0, and (c),(f) +5. Heating pentads are centered at lag days (g) −6, (h) −1, and (i) +4. Dots in each panel represent statistically significant points at 95% level, based on the Monte Carlo resampling method. Vectors in (a)–(c) represent wave activity flux associated with the pentad composite pattern with the reference vector of 7 $m^2 s^{-2}$. Only vectors with magnitude greater than 0.2 $m^2 s^{-2}$ are plotted. The red-lined boxes in (d)–(f) represent the domain of the temperature index (see section 3a). The green-lined boxes in (g)–(i) represent the domain of the heating patch that can induce the PETI circulation pattern (see section 3b). Yellow contours in (h) represent spatially smoothed divergence of the wave activity flux vectors shown in (b). Contours represent ±1 and $\pm 3 \times 10^{-6}$ m s^{-2}, and negative values are dashed.

Far East. Details regarding this temperature analysis follow in section 2c. For latent diabatic heating, we used the JRA-55 reanalysis (Kobayashi et al. 2015) because ERA-Interim only provides a summation of a convective, large-scale condensational and vertical diffusive heating, whereas the JRA-55 reanalysis provides those three variables separately. A previous study has confirmed the similarity between the summation of those three variables from these two reanalysis products (Clark and Feldstein 2020). In addition, circulation indices derived from both datasets have high correlations (Park and Lee 2019, 2021), further justifying the use of both reanalysis datasets. We combined the convective and large-scale condensational heating, vertically averaged from the 950- to 150-hPa level, to define the latent heating (Park and Lee 2019). All data have a 2.5° × 2.5° horizontal resolution and the daily anomaly fields are obtained by removing the seasonal cycle, which is a smoothed calendar day climatology retaining the first 10 harmonics of the cycle. The heating anomaly data have been spatially smoothed by doubly applying the "smth9" function of the NCAR Command Language (version 6.6.2; https://doi.org/10.5065/D6WD3XH5), which uses nine nearby grid points for smoothing.

The circulation trend pattern, although obtained from the long-term trend, varies regionally and fluctuates on an intraseasonal time scale. Therefore, we remove interannual variability and the trends to focus on investigating the intraseasonal time scale process that excites the trend pattern, and how the trend pattern drives the surface temperature signals. The interannual variability, including the trend within the analysis period, is removed by subtracting each year's JJA mean (M. Lee et al. 2017; Kim and Lee 2022).

b. Trend index

To study the dynamical mechanism that drives the Russian Far East and downstream North Pacific trend patterns, we first created an index to identify the days when daily circulation pattern resembles the trend pattern. This index, named as the Russian Far East/Pacific trend index (REP TI), is obtained by projecting the daily circulation field onto the circulation trend pattern, as in the following equation:

$$\mathrm{TI}(t) = \frac{\sum_i \sum_j \psi'^*(\lambda_i, \theta_j, t)\Delta\psi^*(\lambda_i, \theta_j)\cos\theta_j}{\sum_i \sum_j [\Delta\psi^*(\lambda_i, \theta_j)]^2 \cos\theta_j}, \tag{1}$$

where ψ'^* and $\Delta\psi^*$ indicate the 300-hPa daily eddy (zonal-mean removed) streamfunction anomaly and the 300-hPa linear trend pattern of the JJA mean eddy streamfunction (Fig. 1), respectively. The letters λ_i and θ_j indicate longitude and latitude at grid points i and j, respectively, and t refers to JJA days. The projection domain, which corresponds to the REP domain described in section 1 (green box in Fig. 1), ranges from 135°E to 145°W and from 25° to 75°N and is a region where the trend is strong and statistically significant. This trend index therefore measures the similarity between daily circulation field and the circulation trend pattern (Gong et al. 2020; Kim and Lee 2021; Park and Lee 2021). After normalizing this index, we defined positive TI events to be a local peak of this time series with an amplitude greater than 1.0, with individual episodes separated from each other by at least 7 days. We identified 151 positive events based on this procedure.

To test the hypothesis that the upstream Eurasian wave pattern is a factor that influences the REP land surface temperature anomaly, we further conditioned the REP positive TI events by the Eurasian trend index. This Eurasian trend index is identical to the one used by Kim and Lee (2022), which can be obtained by applying the same type of projection in (1) to the Eurasian domain (15°–75°N, 0°–120°E). Specifically, if the composite amplitude of the Eurasian TI, averaged from lag days −7 to −1 of the REP positive trend events, is greater (less) than 0.0, then we defined those REP trend events as positive (negative) conditioned TI events. For brevity, we abbreviate the former as PETI (positive Eurasian-conditioned trend index) and the latter as NETI (negative Eurasian-conditioned trend index). As such, PETI events comprise the days when the REP trend pattern occurs after the Eurasian trend pattern takes place. On the other hand, NETI events belong to a subset of the REP trend events that are preceded by wave trains that oppose the Eurasian trend pattern. Out of the total 151 REP positive trend events, 77 (74) events are categorized as PETI (NETI) events. Based on these two conditions, we make composites of meteorological variables. Their significance levels were tested by the Monte Carlo resampling method that generates random samples with the same number of composites as the PETI and NETI events, for 1000 times.

c. Surface temperature analysis

To diagnose the processes that govern the REP land surface temperature anomalies, we used additional data at the lowest model level of the eta-coordinate system of the ERA-Interim reanalysis, which is a terrain-following hybrid pressure level (ECMWF 2014). The lowest model level is about 10 m above the surface, which can be regarded as the near-surface level (Berrisford et al. 2009). We used this data to compute composites of each term in the thermodynamic energy equation. Following Clark and Feldstein (2020), the perturbation thermodynamic energy equation in the eta-coordinate system can be written as

$$\begin{aligned}\frac{\partial T'}{\partial t} = {} & (-\mathbf{u}' \cdot \nabla\overline{T} + \overline{\mathbf{u}' \cdot \nabla\overline{T}}) + (-\overline{\mathbf{u}} \cdot \nabla T' + \overline{\overline{\mathbf{u}} \cdot \nabla T'}) \\ & + (-\mathbf{u}' \cdot \nabla T' + \overline{\mathbf{u}' \cdot \nabla T'}) + (-\overline{\mathbf{u}} \cdot \nabla\overline{T} + \overline{\overline{\mathbf{u}} \cdot \nabla\overline{T}}) \\ & - \left(\dot{\eta}\frac{\partial T}{\partial \eta}\right)' + \left(\frac{\kappa T\omega}{p}\right)' + Q'_{\mathrm{SW}} + Q'_{\mathrm{LW}} + Q'_{\mathrm{Lat+Mix}} + \mathrm{Res}',\end{aligned} \tag{2}$$

where T and $\mathbf{u}$ are temperature and horizontal wind vector at the lowest model level, respectively. The overbar indicates the seasonal cycle, which is a smoothed calendar day climatology, as discussed above, and a prime denotes the deviation from the seasonal cycle. The left-hand side indicates the perturbation temperature tendency. The first four terms on the right-hand side of (2) indicate anomalous advection of

climatological temperature by the anomalous wind, anomalous advection of anomalous temperature by the climatological wind, anomalous advection of anomalous temperature by the anomalous wind, and a smoothing term, respectively. This smoothing term results from the fact that overbar denotes the smoothed seasonal cycle instead of the more conventional JJA climatological mean, and therefore has a very small nonzero value. In a similar manner, the $\mathbf{u}' \cdot \nabla\overline{T}$ and $\overline{\mathbf{u}} \cdot \nabla T'$ terms are also small and not equal to zero. Since the smoothing term is very small, we do not include it in the main analysis. The fifth term represents anomalous vertical temperature advection, and its numerical computation in the eta-coordinate system is explained in the appendix of Clark and Feldstein (2020). The sixth term is the anomalous temperature tendency due to adiabatic vertical motion, with $\kappa = R_d/c_p$, and ω and p representing vertical velocity and pressure at the lowest model level, respectively. The remaining terms represent diabatic heating due to shortwave radiation, longwave radiation, and the combined effect of latent heating and vertical mixing. We computed the dynamical terms (the first to sixth terms) using data provided by the ERA-Interim, including temperature, horizontal wind, and surface pressure. We computed these terms at 0000, 0600, 1200, and 1800 UTC and averaged them to get the daily mean quantity. The diabatic heating data are obtained directly from the reanalysis except for the $Q'_{\text{Lat+Mix}}$ term, which was determined by subtracting the longwave and the shortwave heating terms from the total diabatic heating. These diabatic heating terms are the daily average of 0000 and 1200 UTC outputs, which are both 12-h accumulated data. The last term in (2) is the residual term that offsets the difference between the summation of the terms on the right-hand side of (2) and the observed temperature tendency. The reasons that these budget terms do not perfectly balance are because ECMWF does not provide horizontal diffusion data and because the analysis increment caused by ECMWF's data assimilation process takes place every 12 h. Also, the dynamic terms are an average of 6-hourly data while the diabatic terms are an average of 12-min time steps (Clark and Feldstein 2020; Clark et al. 2021). Nevertheless, as we will show, this budget analysis reveals the dominant processes responsible for the temperature anomaly development over the REP land region.

We also examined the surface energy budget to diagnose the growth and decay of the skin temperature anomalies. Although skin temperature and surface air temperature are similar, skin temperature refers to the temperature of the ground or ocean surface, not the surface air temperature, which is typically about 2 m above the ground or ocean surface. While their driving mechanisms are different, an analysis of the skin temperature field can help explain the surface air temperature anomaly development. The anomalous skin temperature T'_s can be expressed as

$$T'_s = \frac{F'^{\downarrow}_{\text{lw}} + F'_{\text{sw}} + F'_{\text{sh}} + F'_{\text{lh}} + R'}{4\varepsilon_s \sigma \overline{T}_s^{\,3}}, \tag{3}$$

where ε_s and σ are the emissivity and the Stefan–Boltzmann constant (Lesins et al. 2012; S. Lee et al. 2017; Clark and Feldstein 2020). The prime represents an anomalous quantity. The emissivity is assumed to be 1.0, and $\overline{T}_s$ refers to the JJA mean skin temperature. The terms on the right-hand side of (3) indicate downward longwave radiation, net shortwave radiation, surface sensible heat flux, surface latent heat flux, and the residual term, respectively. The residual term includes effects such as variations of skin temperature associated with sea ice melting and freezing and mixing in the ocean. Therefore, this term tends to be large over the oceanic grid points. Positive values of each term indicate a downward flux.

d. Model setup

We tested the dynamical mechanism implied from our observational analysis by performing idealized model experiments. We used the dry spectral dynamical core from the Geophysical Fluid Dynamics Laboratory, whose setup is identical to that used by Baggett and Lee (2019). The model has topography with a horizontal triangular 42 resolution and 28 vertical sigma levels. Also, this model uses fourth-order horizontal diffusion, a damping time scale of 0.1 days at its smallest length scale, Newtonian cooling, and a Rayleigh friction parameterization adapted from Held and Suarez (1994). We perform initial-value model calculations, which is a useful method for examining the atmospheric response to a specified forcing for a particular background field, which we take to be the JJA climatology of the zonal and meridional wind, surface pressure, and temperature for the period of 1979–2017. Since the climatological flow is not a steady-state solution to the model's equations, to keep the climatological flow as the model's initial state while preventing model solution from drifting from that initial state, we need an additional forcing term, which can be obtained by integrating the model equations forward by a one-time step. With this forcing term introduced into the model's equations, the model solution will evolve only when an additional forcing is imposed (Franzke et al. 2004). The additional forcing applied to the model is the time-evolving lagged composite of the heating anomalies whose vertical level is interpolated into the idealized model's 28 sigma levels (Park and Lee 2019). On model day 1, the lag day −10 heating composite is imposed, and on day 2, the lag day −9 composite is imposed, and so on. The forcing is applied until model day 17, which corresponds to lag day +6 in the observational data.

3. Results

a. Structure of the PETI and NETI composites

The PETI pentad composite of the 300-hPa streamfunction anomalies shows circulation anomalies over Eurasia that resemble the Eurasian trend pattern (15°–75°N, 0°–120°E in Fig. 1) from lag days −7 to −3 (Fig. 2a). The wave activity flux vectors (Takaya and Nakamura 2001) show propagation from Europe to East Asia and they converge near 65°N, 150°E where a weak anticyclone is located. This Eurasian trend pattern dissipates and the REP trend pattern develops from lag days −2 to +2 (Fig. 2b). During this period, wave activity flux

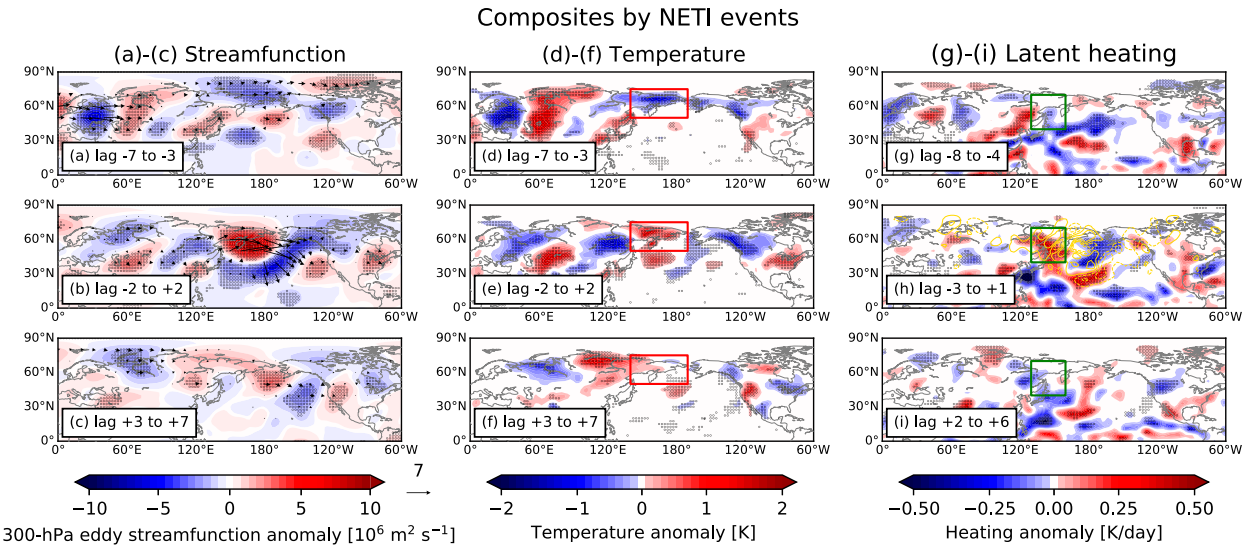

FIG. 3. As in Fig. 2, but for NETI events. Pentad composites of the (left) 300-hPa eddy streamfunction anomaly, (center) temperature anomaly at the lowest level of the eta coordinate, and (right) latent heating anomaly during NETI events. Streamfunction and temperature pentads are centered at lag days (a),(d) −5, (b),(e) 0, and (c),(f) +5. Heating pentads are centered at lag days (g) −6, (h) −1, and (i) +4. Dots in each panel represent statistically significant points at 95% level, based on the Monte Carlo resampling method. Vectors in (a)–(c) represents wave activity flux associated with the pentad composite pattern with the reference vector of 7 $m^2 s^{-2}$. Only vectors with magnitude greater than 0.2 $m^2 s^{-2}$ are plotted. The red-lined boxes in (d)–(f) represent the domain of the temperature index (see section 3a). The green-lined boxes in (g)–(i) represent the domain of the heating patch that can induce the NETI circulation pattern (see section 3b). Yellow contours in (h) represent spatially smoothed divergence of the wave activity flux vectors shown in (b). Contours represent ±1 and ±3 × 10^{-6} m s^{-2}, and negative values are dashed.

vectors emanate from around 65°N, 150°E, instead of propagating from Eurasia. These behaviors of the wave activity flux vectors imply that during the initial stage from lag days −7 to −3 the weak anticyclone near 150°E can be understood as arising from downstream propagation of the Eurasian trend pattern, while the strong anticyclone during the peak of the events (from lag days −2 to +2) is part of a separately excited wave train with wave forcing located near the Russian Far East. Most of the circulation signals decay after lag day +3 (Fig. 2c). During the development stage of the NETI events (from lag days −7 to −3; Fig. 3a), the 300-hPa streamfunction composite anomalies oppose the Eurasian circulation trend pattern with negative streamfunction anomalies to the north of Kamchatka Peninsula, which is opposite to the PETI composite pattern (cf. Figs. 2a and 3a). From lag days −2 to +2, the Eurasian circulation anomalies weaken and the REP trend pattern develops with a new group of wave activity flux vectors emanating from the Russian Far East (Fig. 3b). This circulation behavior is similar to those of PETI events, suggesting that the REP trend pattern is a separately forced wave rather than this pattern arising from downstream propagation associated with the Eurasian trend pattern. The NETI circulation pattern also decays after lag day +3 (Fig. 3c).

During the initial stage of the PETI events, the surface temperature over the REP land region is anomalously positive (red-lined box in Fig. 2d). This temperature anomaly intensifies during the peak of the events (Fig. 2e) and decays after lag +3 (Fig. 2f). However, during NETI events, the REP land temperature anomaly is initially negative from lag days −7 to −3 (red-lined box in Fig. 3d). As the anticyclone develops over that region, at the peak of the events, the temperature anomaly becomes positive (Fig. 3e), but with a smaller magnitude than that of PETI events. The NETI temperature anomaly also decays after lag day +3 (Fig. 3f).

These differences between the two groups can also be quantified by compositing three indices, the Eurasian trend index (TI), the REP TI, and the REP land temperature index. The temperature index is the spatially averaged daily temperature anomaly over the domain 50°–75°N, 140°E–170°W (red-lined boxes in Figs. 2d–f and 3d–f). The REP land temperature index is then normalized and composited for the PETI and NETI events. Figure 4 shows the composite amplitudes of those three indices for the PETI (left panel) and NETI (right panel) events. During the PETI events, Eurasian TI amplitudes are positive and statistically significant from lag day −10 to 0, which is expected by the construction of PETI events (red line in Fig. 4a). The statistically significant REP TI amplitudes occurs from lag days −3 to +4 (blue line in Fig. 4a). During NETI events, the Eurasian TI amplitudes are initially negative with statistically significant values occurring from lag days −8 to 0, which is again expected by the definition of NETI events (red line in Fig. 4b). Statistically significant REP TI amplitudes take place from lag days −4 to +3 (blue line in Fig. 4b). The composite amplitudes of the REP TI are very similar for both conditions and statistically significant anomalies also occur during similar lag days. This implies that the REP trend pattern is, on average, unrelated to the Eurasian trend pattern. However, there is a clear

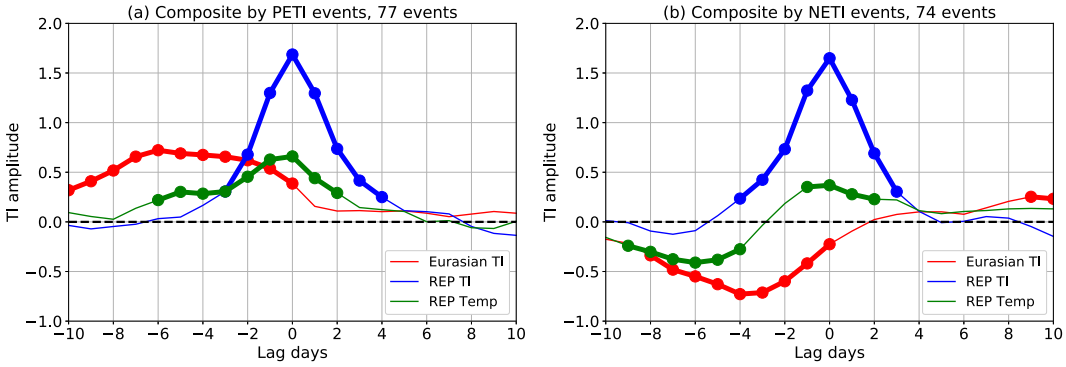

FIG. 4. Composite of the Eurasian trend index (red), the REP trend index (blue), and the REP land temperature index (green) during (a) PETI and (b) NETI events. Dots with thick lines indicate statistically significant values at 95% level computed by the Monte Carlo resampling method.

difference in the temperature index. The statistically significant positive temperature anomalies take places from lag days −6 to +2 during PETI events (green line in Fig. 4a). However, during NETI events, the initial temperature anomalies are negative (from lag days −9 to −4) and statistically significant weak positive anomalies occur only from lag days −1 to +2 (green line in Fig. 4b).

The composite structures indicate that the initial temperature anomalies show opposite signs depending on the phase of the upstream Eurasian trend pattern. While the amplification of temperature anomaly from about lag day −3 onward is associated with the development of the anticyclone of the REP trend pattern for both PETI and NETI events, the difference in the initial condition could influence the relative strength and the persistence of the positive temperature anomaly over the Russian Far East. Therefore, we investigate the role of the upstream circulation in determining the initial temperature anomaly. This question is addressed by analyzing composites of each term of the thermodynamic energy equation in section 3c.

b. *Role of latent heating anomalies and model experiment*

For both PETI and NETI events, there are enhanced latent heating anomalies near the Yakutia region (green-lined boxes in Figs. 2g,h and 3h). These latent heating anomalies begin at earlier lags for the PETI events, and for both events the latent heating anomalies have dissipated by lag day +2 (Figs. 2i and 3i). The location of these heating anomalies is to the west of the prominent Russian Far East anticyclone, where the wave activity flux divergence occurs (yellow contours in Figs. 2h and 3h). Given that these heating anomalies mostly occur during early stage and that enhanced diabatic heating anomalies play an important role in the formation of extratropical upper-level anticyclones (Hoskins and Karoly 1981; Pfahl et al. 2015; Steinfeld and Pfahl 2019), we hypothesize that some of these latent heating anomalies can excite the REP trend pattern. To test this hypothesis, we conducted a set of idealized model experiments using the model described in section 2d. In this experiment, the model is forced with observed PETI and NETI heating composites. The model solutions will be compared with the observed REP trend pattern.

To identify the primary forcing region, we performed a set of experiments by systematically varying the location of the composite heating that forces the model (Branstator 1985; Kim and Lee 2021). Each heating location is defined with a patch of 30° latitude × 30° longitude. For each simulation, the patch location is varied by a 10° increment in both the latitudinal and longitudinal directions. For example, in the first model run with the PETI heating composite, the model is forced with the heating composite located over 30°S–0°, 0°–30°E. The heating anomalies at all other grid points are set to be zero. The next simulation uses the patch located over 30°S–0°, 10°–40°E. Accordingly, there are 36 available patches in the longitudinal direction for this 30°S–0° band. The next latitudinal band is 20°S–10°N, which again has 36 possible patches in the longitudinal direction. Since there are 10 latitudinal bands to cover the entire tropics and the Northern Hemisphere (from the 30°S–0° band to the 60°–90°N band), we conducted a total of 360 model simulations to cover all possible PETI patch domains. We then performed another set of 360 experiments using the NETI heating composite patches.

For each of those simulations, we evaluated if the model response resembles the REP trend pattern by projecting the model response onto the observed composite pattern (Kim and Lee 2022):

$$\text{Proj} = \frac{\sum_i \sum_j \overline{\psi'^{*}_{\text{mod}}}(\lambda_i, \theta_j)\, \overline{\psi'^{*}_{\text{obs}}}\,(\lambda_i, \theta_j)\cos(\theta_j)}{\sum_i \sum_j [\overline{\psi'^{*}_{\text{obs}}}\,(\lambda_i, \theta_j)]^2 \cos(\theta_j)}. \tag{4}$$

The projection domain ranges from 25° to 75°N and from 135°E to 145°W, which is the same range used for constructing the REP trend index. Here, ψ'^{*}_{mod} is the 300-hPa model eddy streamfunction response averaged from model days 8 to 14. The input forcing is the daily time-evolving heating composites from lag day −10. Therefore, model days 8 to 14 correspond to the observed composite lag days from −3 to +3. Accordingly, $\overline{\psi'^{*}_{\text{obs}}}$, which is the observed eddy streamfunction

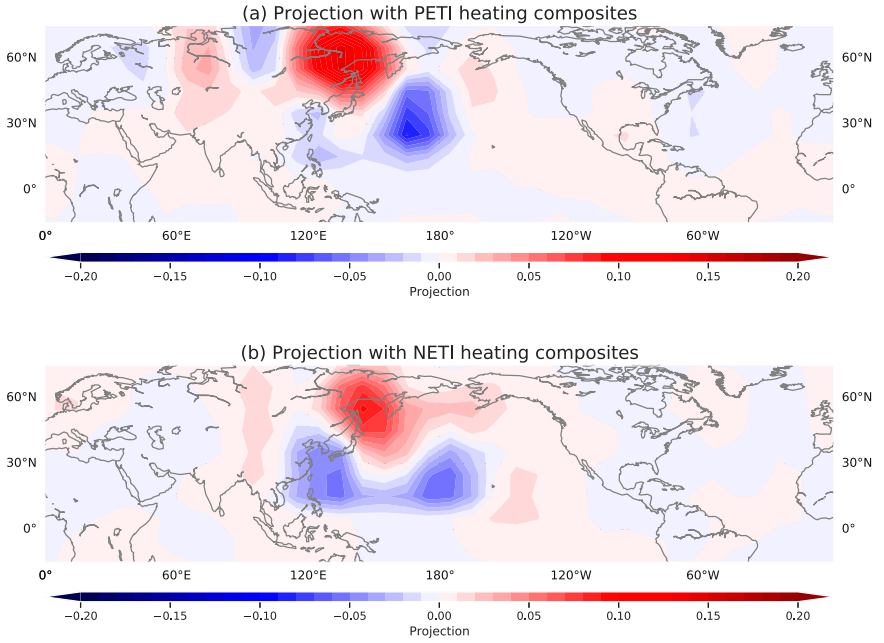

FIG. 5. Projection results from 360 model patch experiments using (a) PETI and (b) NETI heating composites. Positive (negative) projection values, or red (blue) shadings, indicate that the heating composite located at that grid point can induce the circulation pattern that matches with (opposes) the observed composite pattern. See section 3b for details.

composite at the 300-hPa level, is also averaged from lag days −3 to +3. These 300-hPa streamfunction composites (contours in Figs. 6a and 6b) are similar to the composite fields in Figs. 2b and 3b, that is, the PETI (NETI) composite streamfunction patterns, respectively, except for the inclusion of lag days −3 and +3. These lag days are the time period when the composite of the REP trend index is statistically significant (blue lines in Figs. 4a and 4b). For the simulations with the PETI (NETI) heating composite, we projected the model responses onto the PETI (NETI) composite streamfunction pattern. Positive projection values in (4) therefore indicate that the model response resembles the observed composite pattern. For all 360 simulations, we computed the projection value and assigned it to the grid point centered at the corresponding patch forcing. For example, the projection value obtained from the simulation with a patch domain of 30°S–0°, 0°–30°E is assigned to the grid point of 15°S, 15°E. The results are plotted in Fig. 5. The red (blue) shadings indicate positive (negative) projection values, and thus heating anomalies centered at that region excite the model response that resembles (opposes) the REP trend pattern.

Figure 5a indicates that the heating anomalies centered at the Yakutia region can excite the REP trend pattern. Specifically, the patch domain of 50°–80°N and 120°–150°E (the green-lined boxes in Figs. 2g–i and 6a) can induce the REP trend pattern with a prominent anticyclone centered near the Kamchatka Peninsula (shadings in Fig. 6a). The downstream cyclonic response over the North Pacific and high latitudes of North America also resembles the overlaid contours of the PETI streamfunction composite. The NETI heating anomaly over the Yakutia region is also capable of generating the REP trend pattern (Fig. 5b). The NETI heating anomaly centered at 40°–70°N and 130°–160°E (the green-lined box in Figs. 3g–i and 6b) induces the response (shading) that resembles the NETI streamfunction composite pattern (contours in Fig. 6b). The overall model results indicate that the REP trend pattern can be induced by enhanced latent heating anomalies centered over the Yakutia region. In addition, given the similarity between the model responses to both PETI and NETI heating composites, these results suggest that the latent heating-induced mechanism for generating the REP trend pattern is rather independent from the phase of the upstream Eurasian trend pattern.

c. *Thermodynamic energy budget analysis*

While the REP trend pattern and its excitation mechanism are independent from the Eurasian trend pattern, the initial condition of the surface temperature anomalies behave differently depending on the phase of the Eurasian trend pattern. In this subsection, we investigate the mechanism that drives the surface temperature anomalies over the REP land region and how it is related to the upstream Eurasian trend pattern. As mentioned in section 2c, thermodynamic energy budget diagnostics can reveal the dominant process responsible for the temperature anomaly growth. We therefore have composited each term in (2) and compared them with the observed temperature tendency. Each component of the thermodynamic equation is spatially averaged over the domain of 50°–75°N, 140°E–170°W (the red-lined boxes in Figs. 2d–f and 3d–f)

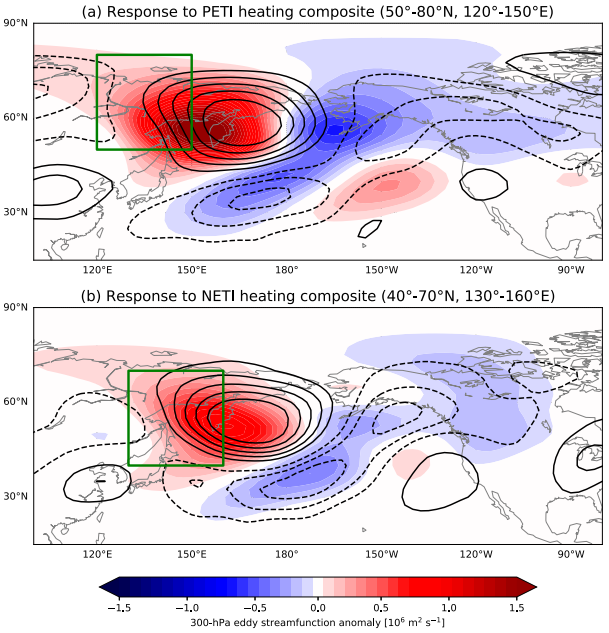

FIG. 6. Shadings represent the 300-hPa model eddy streamfunction response, averaged from model days 8 to 14, forced by the heating anomaly located over the green-lined box. Contours are the observed streamfunction composites at 300-hPa level averaged from lag days −3 to +3, with an interval of 1.0×10^6 m^2 s^{-1}. The upper (lower) panel shows the result based on the composites during PETI (NETI) events. Green boxes represent the patch domain with the greatest projection value from Fig. 5.

before being composited. Therefore, the resulting line plot shows the daily evolution of the anomalous temperature tendency in the REP land region and how much each process contributes to the temperature tendency.

The anomalous temperature tendency during PETI events is characterized by double peaks with the first peak occurring at lag day −7 and a second stronger peak following at lag day −2 (black dashed line in Fig. 7a). The gray dashed line, which is the summation of all terms on the right-hand-side terms of (2), largely resembles the observed tendency, indicating that the thermodynamic budget is accurate enough to be used to investigate the dominant growth and decay processes. The first growth from lag days −7 to −4 is mostly caused by the anomalous advection of the climatological temperature by the anomalous wind (green line). This warm air advection is influenced by anomalous southwesterly winds near 130°E, which enter at the western corner of the target domain (red-lined box in Fig. 8a). These southwesterly winds are located at the eastern flank of the Siberian cyclone (vectors in Fig. 8a and shadings in Fig. 2a). Given the fact that wave activity flux vectors propagate from Europe to the Russian Far East during the initial stage of the PETI events (Fig. 2a), this Siberian cyclonic circulation is likely the result of downstream propagation associated with the Eurasian circulation trend pattern. In addition, the weak anticyclonic circulation over the Russian Far East during the initial stage (Fig. 2a), which also arises from the downstream propagation of the Eurasian trend pattern, further induces the positive temperature tendency over that region by allowing more shortwave radiation to reach the near-surface atmosphere (red line in Fig. 7a and shadings in Fig. 8g). Therefore, the initial development of the warm temperature anomalies is induced by the downstream wave pattern of the Eurasian circulation trend pattern. As the REP trend pattern develops, although the area-averaged value of the shortwave radiation may slightly weaken from lag days −4 to 0 (red line in Fig. 7a), it still contributes to the warming over the eastern half of the target domain during this time period (Fig. 8h). From lag day −5 onward, adiabatic warming, driven by the downward motion within the anticyclone (green contours in Fig. 8f), becomes the dominant factor for the temperature growth and drives the second and major peak of the temperature tendency curve (yellow line in Fig. 7a and shadings in Fig. 8f).

The advection of the anomalous temperature by climatological wind acts to reduce the temperature, with statistically significant anomalies from lag days −10 to −9 and from −2 to +2 (light blue line in Fig. 7a and shadings in Figs. 8c,d). This anomalous decay is likely an enhancement of the climatological process. Climatologically, the JJA temperature over the REP land is a local maximum with the surrounding ocean temperature being cooler. The southerly climatological winds (vectors in Figs. 8c,d) advect cool oceanic air toward the land. Therefore, the advection of the climatological temperature by the climatological wind over this domain is negative (not shown). A positive temperature perturbation over the land would strengthen the climatological temperature gradient between the land and the ocean, and therefore result in a stronger cold air advection by the climatological wind, as shown in Figs. 8c and 8d.

During the NETI events, the temperature tendency, which starts with negative values, becomes positive at lag day −6 and peaks at lag day −3 (black dashed line in Fig. 9a). These positive tendencies are primarily driven by three terms in the temperature advection. The advection of the anomalous temperature by the climatological wind first initiates the positive temperature tendency from lag days −6 to −5 (light blue line in Fig. 9a). This is a response to the initial negative temperature anomaly over the land that weakens the climatological land–sea temperature gradient. From lag day −4 to −2, as the wind anomalies associated with the REP trend pattern develop, advection of both the climatological and anomalous temperature by the anomalous wind drives an even stronger positive temperature tendency (green and purple lines in Fig. 9a). As in the PETI events, the adiabatic term also contributes to the warming (yellow line in Fig. 9a) because of downward motion over the Russian Far East anticyclone. These results indicate that, once the Russian Far East anticyclone develops, the surface temperature anomalies generally grow by adiabatic warming. However, without the initial warm anomaly driven remotely by the upstream wave as in PETI events, this process alone would be unable to generate the large and persistent temperature anomaly.

The cooling effect by longwave radiation shows a stark difference between the PETI and NETI events, being more pronounced in the latter (blue lines in Figs. 7a and 9a). The skin

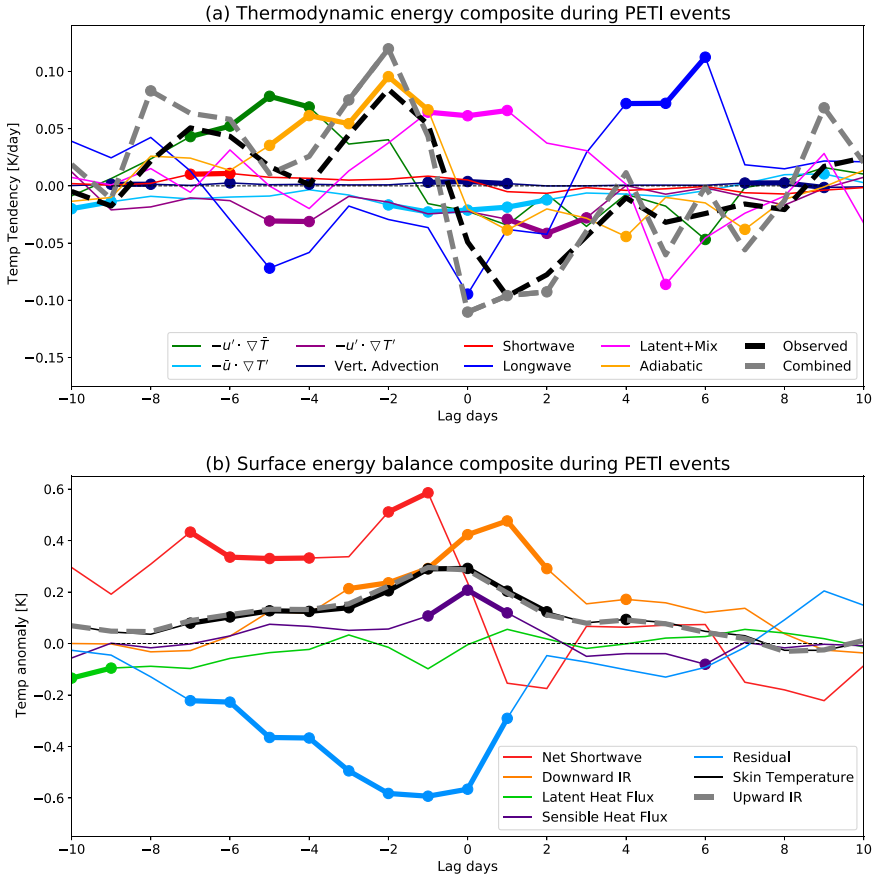

FIG. 7. (a) Composite of each term in the thermodynamic energy equation during PETI events. Each colored line represents the contribution by the indicated term to the development of the REP land temperature tendency. Green, light blue, purple, and dark blue lines represent three different components of the horizontal temperature advection and the vertical advection, respectively. Red, blue, pink, and yellow lines represent three different components of the diabatic heating and adiabatic warming, respectively. The gray-dashed line represents combination of above-mentioned terms, and the black-dashed line is the observed temperature tendency. (b) Composite of each term in the surface energy balance equation during PETI events. The black line indicates the skin temperature anomalies. Red, orange, light green, purple, gray-dashed, and light blue lines represent the skin temperature anomaly contributed by the net shortwave flux, downward IR, latent heat flux, surface sensible heat flux, upward IR, and the residual term, respectively. Dots with thick lines in both panels represent statistically significant points at the 90% level as computed by the Monte Carlo resampling method.

temperature evolution offers an explanation for this difference. Figure 7b shows that during the PETI events, the initial growth of the skin temperature anomalies (black line) is mostly driven by net shortwave radiation (red line) with negligible contribution by the latent (green line) and sensible (purple line) heat fluxes and a negative contribution by the residual term (blue line). This is due to the presence of the anomalous anticyclonic circulation over the Russian Far East region during the PETI events (Figs. 2a and 2b). A surface with anomalously high skin temperature emits more longwave radiation upward into the atmosphere. [The anomalous upward longwave flux (gray-dashed line) is almost indistinguishable from the skin temperature anomaly (black line).] Therefore, while the warmer atmosphere during the PETI events cools by emitting more longwave radiation, the longwave radiative flux from the surface warms the atmosphere, compensating for the cooling. Indeed, there is no notable divergence of longwave radiative flux out of the atmospheric layer centered at the lowest model level. This is likely to contribute to the PETI warm anomaly being more persistent and stronger. During the NETI events (Fig. 9b), however, initial skin temperature anomalies are either negative or close to zero (black line), owing to the negative anomalies of downward infrared radiation (orange line) and the net shortwave fluxes (red line). This initially negative skin temperature anomaly produces a muted longwave flux from ground to the atmosphere, hence allowing for a stronger emission of longwave radiation from the atmosphere.

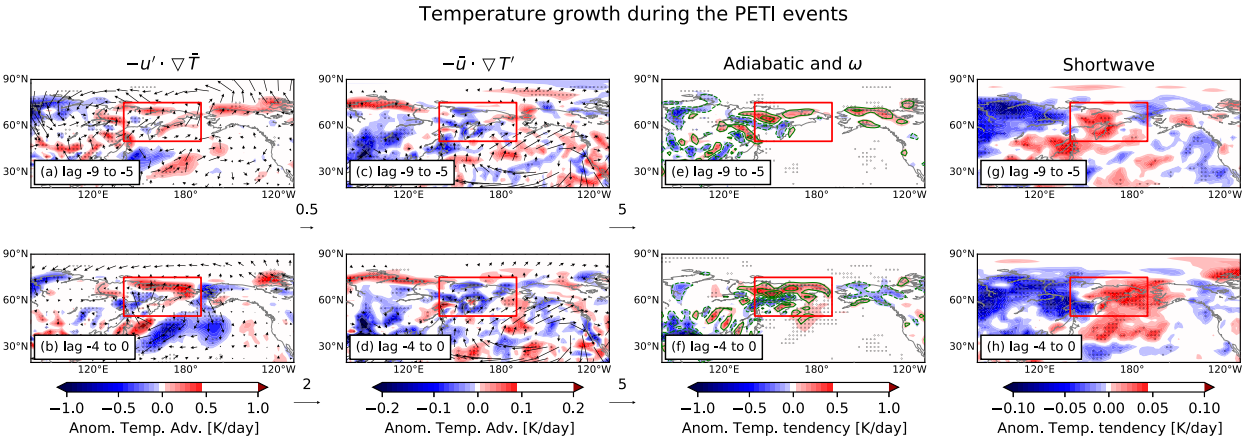

FIG. 8. Pentad composites of temperature tendency driven by (first column) $-\mathbf{u}' \cdot \nabla \overline{T}$, (second column) $-\overline{\mathbf{u}} \cdot \nabla T'$, (third column) adiabatic process, and (fourth column) shortwave radiation during PETI events. Pentad composites are centered at (top) lag day −7 and (bottom) lag day −2. (a),(b) Vectors represent pentad composites of anomalous wind at the lowest model level with the reference vector of 0.5 m s^{-1} in (a) and 2 m s^{-1} in (b). Vectors with magnitude less than 0.05 m s^{-1} are omitted. (c),(d) Vectors represent the JJA climatological winds at the lowest model level with the reference vector of 5 m s^{-1}. Only vectors with magnitude greater than 0.5 m s^{-1} are plotted. (e),(f) Contours represent pentad composites of anomalous vertical wind (ω) at the lowest model level. Contours represent ±2, ±6, and $\pm 10 \times 10^{-3}$ Pa s^{-1}. Negative values are dashed. Dots represent statistically significant points of anomalous temperature tendencies at 95% level as computed by the Monte Carlo resampling method. Red-lined boxes are the REP land temperature domain. Note that each variable has different color bar ranges.

4. Conclusions and discussion

We investigated the dynamical mechanism that drive the REP circulation trend pattern and associated surface temperature anomalies over the REP land region on the intraseasonal time scale. The REP trend pattern is found to be driven by positive latent heating anomalies over the Yakutia region, which is to the west of the anticyclone near the Kamchatka Peninsula. However, this wave pattern, on its own, is unable to induce a strong surface temperature anomaly. Instead, the anomalously warm surface hinges on the presence of the upstream Eurasian trend pattern. The near-surface circulation associated with the Eurasian circulation trend pattern generates warm advection, initiating the warm anomaly over the REP land region. Once the REP trend pattern develops, a few days after the onset of the positive temperature anomaly, the anticyclone over the REP land region further enhances the temperature anomaly through descending motion, which warms the surface air adiabatically. Without such an initial condition, the REP trend pattern alone cannot induce persistent strong temperature anomalies.

Unlike the Eurasian trend pattern, which is known to be related to strong surface temperature anomalies over central and eastern Europe, we found that the REP trend pattern on its own cannot produce strong and persistent temperature anomalies. One possible reason is that while the Eurasian trend pattern is quasi-stationary, the REP trend pattern is relatively transient. Kim and Lee (2022) showed that the Eurasian trend pattern associated with strong temperature anomaly is generated by upstream quasi-stationary heating anomalies that persist for about 10 days prior to the development of the wave pattern. However, the heating anomalies responsible for the REP trend pattern are statistically significant for only 4–6 days (not shown). With such a relatively transient forcing, the associated wave pattern may not be persistent long enough to have a strong influence on the surface weather. In addition, heating anomalies located over the subtropical North Pacific generate circulation anomalies that negatively project onto the trend pattern (blue shadings in Figs. 5a and 5b). In contrast, for the Eurasian trend pattern with strong temperature anomalies, there are no heating anomalies that act to cancel out the Eurasian trend pattern (see Fig. 5a of Kim and Lee 2022). These findings suggest that the characteristics of heating anomalies play an important role in the strength and the persistence of the circulation anomalies and, hence, the surface temperature anomalies.

While latent heating anomalies play an important role in exciting the REP trend pattern on an intraseasonal time scale, it is unclear whether latent heating also contributes to the long-term trend of the circulation. Kim and Lee (2022) found that the intraseasonal latent heating anomalies, responsible for exciting the Eurasian trend pattern, have been trending upward. This result indicates that the long-term trend of the Eurasian trend pattern was contributed by the upward heating trend. We investigated whether latent heating anomalies located over the Yakutia region have played a similar role in the long-term trend. We found that while the latent heating over Yakutia have trended upward, its contribution to the circulation trend has been weak. Therefore, we conclude that the latent heating trend is insufficient to explain how the REP pattern has emerged in the long-term trend, and that further analysis is necessary to answer this question. Instead, the findings of this study are helpful for improving weather forecasts and the subseasonal-to-seasonal prediction of heat waves over the Russian Far East.

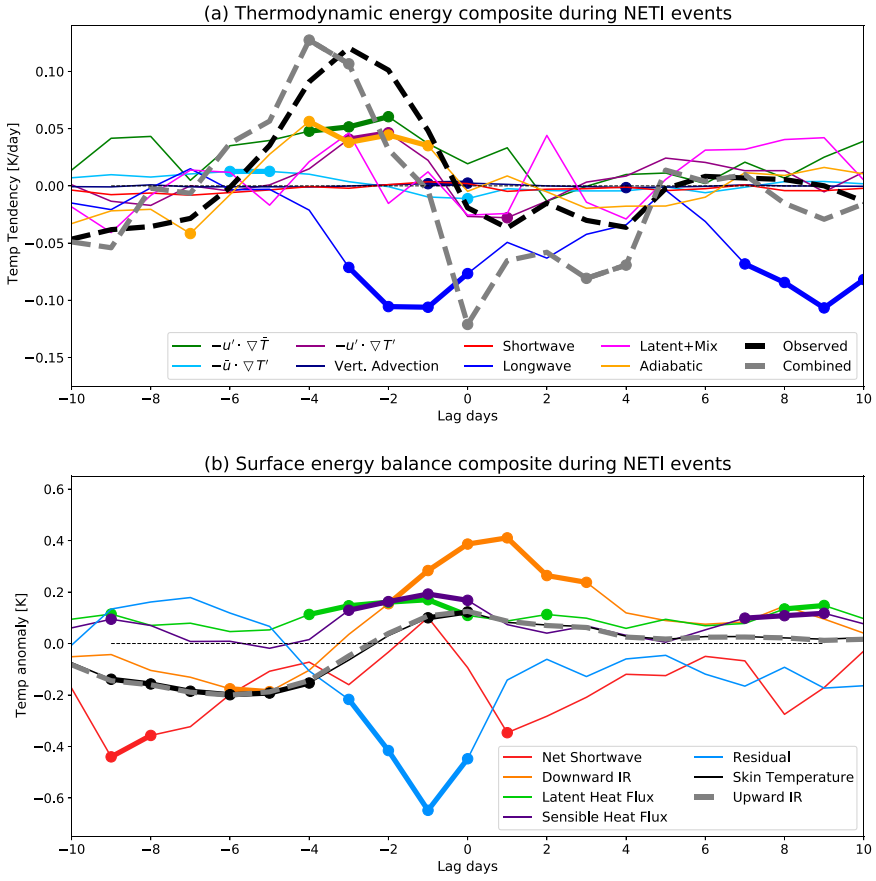

FIG. 9. As in Fig. 7, but for NETI events. (a) Composite of each term in the thermodynamic energy equation during NETI events. Each colored line represents the contribution by the indicated term to the development of the REP land temperature tendency. Green, light blue, purple, and dark blue lines represent three different components of the horizontal temperature advection and the vertical advection, respectively. Red, blue, pink, and yellow lines represent three different components of the diabatic heating and adiabatic warming, respectively. The gray-dashed line represents a combination of above-mentioned terms, and the black-dashed line is the observed temperature tendency. (b) Composite of each term in the surface energy balance equation during NETI events. The black line indicates the skin temperature anomalies. Red, orange, light green, purple, gray-dashed, and light blue lines represent the skin temperature anomaly contributed by the net shortwave flux, downward IR, latent heat flux, surface sensible heat flux, upward IR, and the residual term, respectively. Dots with thick lines in both panels represent statistically significant points at the 90% level as computed by the Monte Carlo resampling method.

The different dynamical characteristics of the Eurasian and REP trend patterns suggest that the observed summer circulation trend pattern comprises multiple wave trains that fluctuate on their own intraseasonal time scales. The findings from this study and from Kim and Lee (2021, 2022) indicate that extratropical latent heating anomalies generate circulation patterns confined to the region of the forcing and its immediate downstream rather than the hemisphere-wide wave train. These results do not conform to the idea of quasi-resonant amplification (Petoukhov et al. 2013; Kornhuber et al. 2020), which attributes the recent co-occurrence of heat waves to an amplified hemispheric wave pattern. Instead, our findings suggest that the trend pattern, although it may resemble the circumglobal teleconnection pattern (CGT; Branstator 2002; Ding and Wang 2005; Teng et al. 2013, 2019; Baker et al. 2019), arises from a combination of upward trends of multiple wave trains rather than being caused by the trend of a single CGT-like wave train.

Acknowledgments. We thank Steven Feldstein, Cory Baggett, Mingyu Park, Joseph Clark, and Allen Mewhinney for their discussion on this research. This research was funded by National Science Foundation Grant AGS-1948667.

Data availability statement. The ERA-Interim reanalysis data are publicly accessible in the ECMWF's webpage

(https://www.ecmwf.int/en/forecasts/datasets/reanalysis-datasets/era-interim), and the JRA-55 reanalysis can be downloaded at NCAR's Research Data Archive (https://rda.ucar.edu/).

REFERENCES

Baggett, C., and S. Lee, 2019: Summertime midlatitude weather and climate extremes induced by moisture intrusions to the west of Greenland. *Quart. J. Roy. Meteor. Soc.*, **145**, 3148–3160, https://doi.org/10.1002/qj.3610.

Baker, H. S., T. Woollings, C. Mbengue, M. R. Allen, C. H. O'Reilly, H. Shiogama, and S. Sparrow, 2019: Forced summer stationary waves: The opposing effects of direct radiative forcing and sea surface warming. *Climate Dyn.*, **53**, 4291–4309, https://doi.org/10.1007/s00382-019-04786-1.

Berrisford, P., D. Dee, K. Fielding, M. Fuentes, P. Kallberg, S. Kobayashi, and S. Uppala, 2009: The ERA Interim archive: Version 1.0. ECMWF ERA Rep., ECMWF, Reading, United Kingdom, 16 pp., https://www.ecmwf.int/node/8173.

Branstator, G., 1985: Analysis of general circulation model sea-surface temperature anomaly simulations using a linear model. Part I: Forced solutions. *J. Atmos. Sci.*, **42**, 2225–2241, https://doi.org/10.1175/1520-0469(1985)042<2225:AOGCMS>2.0.CO;2.

——, 2002: Circumglobal teleconnections, the jet stream waveguide, and the North Atlantic Oscillation. *J. Climate*, **15**, 1893–1910, https://doi.org/10.1175/1520-0442(2002)015<1893:CTTJSW>2.0.CO;2.

Clark, J. P., and S. B. Feldstein, 2020: What drives the North Atlantic Oscillation's surface air temperature anomaly pattern? Part II: A decomposition of the surface downward longwave radiation anomalies. *J. Atmos. Sci.*, **77**, 199–216, https://doi.org/10.1175/JAS-D-19-0028.1.

——, V. Shenoy, S. B. Feldstein, S. Lee, and M. Goss, 2021: The role of horizontal temperature advection in Arctic amplification. *J. Climate*, **34**, 2957–2976, https://doi.org/10.1175/JCLI-D-19-0937.1.

Dee, D. P., and Coauthors, 2011: The ERA-Interim reanalysis: Configuration and performance of the data assimilation system. *Quart. J. Roy. Meteor. Soc.*, **137**, 553–597, https://doi.org/10.1002/qj.828.

Ding, Q., and B. Wang, 2005: Circumglobal teleconnection in the Northern Hemisphere summer. *J. Climate*, **18**, 3483–3505, https://doi.org/10.1175/JCLI3473.1.

ECMWF, 2014: IFS documentation—Cy40r1 Part III: Dynamics and numerical procedures. ECMWF, 29 pp., https://www.ecmwf.int/node/9203.

Enomoto, T., B. J. Hoskins, and Y. Matsuda, 2003: The formation mechanism of the Bonin high in August. *Quart. J. Roy. Meteor. Soc.*, **129**, 157–178, https://doi.org/10.1256/qj.01.211.

Franzke, C., S. Lee, and S. B. Feldstein, 2004: Is the North Atlantic Oscillation a breaking wave? *J. Atmos. Sci.*, **61**, 145–160, https://doi.org/10.1175/1520-0469(2004)061<0145:ITNAOA>2.0.CO;2.

Gong, T., S. B. Feldstein, and S. Lee, 2020: Rossby wave propagation from the Arctic into the midlatitudes: Does it arise from in situ latent heating or a trans-Arctic wave train? *J. Climate*, **33**, 3619–3633, https://doi.org/10.1175/JCLI-D-18-0780.1.

Held, I. M., and M. J. Suarez, 1994: A proposal for the intercomparison of the dynamical cores of atmospheric general circulation models. *Bull. Amer. Meteor. Soc.*, **75**, 1825–1830, https://doi.org/10.1175/1520-0477(1994)075<1825:APFTIO>2.0.CO;2.

Hoskins, B. J., and D. J. Karoly, 1981: The steady linear response of a spherical atmosphere to thermal and orographic forcing. *J. Atmos. Sci.*, **38**, 1179–1196, https://doi.org/10.1175/1520-0469(1981)038<1179:TSLROA>2.0.CO;2.

——, and T. Ambrizzi, 1993: Rossby wave propagation on a realistic longitudinally varying flow. *J. Atmos. Sci.*, **50**, 1661–1671, https://doi.org/10.1175/1520-0469(1993)050<1661:RWPOAR>2.0.CO;2.

Kim, D. W., and S. Lee, 2021: Relationship between boreal summer circulation trend and destructive stationary–transient wave interference in the western hemisphere. *J. Climate*, **34**, 4989–4999, https://doi.org/10.1175/JCLI-D-20-0530.1.

——, and ——, 2022: The role of latent heating anomalies in exciting the summertime Eurasian circulation trend pattern and high surface temperature. *J. Climate*, **35**, 801–804, https://doi.org/10.1175/JCLI-D-21-0392.1.

Kobayashi, S., and Coauthors, 2015: The JRA-55 reanalysis: General specifications and basic characteristics. *J. Meteor. Soc. Japan*, **93**, 5–48, https://doi.org/10.2151/jmsj.2015-001.

Kornhuber, K., D. Coumou, E. Vogel, C. Lesk, J. F. Donges, J. Lehmann, and R. M. Horton, 2020: Amplified Rossby waves enhance risk of concurrent heatwaves in major breadbasket regions. *Nat. Climate Change*, **10**, 48–53, https://doi.org/10.1038/s41558-019-0637-z.

Lee, M. H., S. Lee, H. J. Song, and C. H. Ho, 2017: The recent increase in the occurrence of a boreal summer teleconnection and its relationship with temperature extremes. *J. Climate*, **30**, 7493–7504, https://doi.org/10.1175/JCLI-D-16-0094.1.

Lee, S., T. Gong, S. B. Feldstein, J. A. Screen, and I. Simmonds, 2017: Revisiting the cause of the 1989–2009 Arctic surface warming using the surface energy budget: Downward infrared radiation dominates the surface fluxes. *Geophys. Res. Lett.*, **44**, 10 654–10 661, https://doi.org/10.1002/2017GL075375.

Lesins, G., T. J. Duck, and J. R. Drummond, 2012: Surface energy balance framework for Arctic amplification of climate change. *J. Climate*, **25**, 8277–8288, https://doi.org/10.1175/JCLI-D-11-00711.1.

Park, M., and S. Lee, 2019: Relationship between tropical and extratropical diabatic heating and their impact on stationary–transient wave interference. *J. Atmos. Sci.*, **76**, 2617–2633, https://doi.org/10.1175/JAS-D-18-0371.1.

——, and ——, 2021: The role of planetary-scale eddies on the recent isentropic slope trend during boreal winter. *J. Atmos. Sci.*, **78**, 2879–2894, https://doi.org/10.1175/JAS-D-20-0348.1.

Petoukhov, V., S. Rahmstorf, S. Petri, and H. J. Schellnhuber, 2013: Quasiresonant amplification of planetary waves and recent Northern Hemisphere weather extremes. *Proc. Natl. Acad. Sci. USA*, **110**, 5336–5341, https://doi.org/10.1073/pnas.1222000110.

Pfahl, S., C. Schwierz, M. Croci-Maspoli, C. M. Grams, and H. Wernli, 2015: Importance of latent heat release in ascending air streams for atmospheric blocking. *Nat. Geosci.*, **8**, 610–615, https://doi.org/10.1038/ngeo2487.

Schubert, S., H. Wang, R. Koster, M. Suarez, and P. Groisman, 2014: Northern Eurasian heat waves and droughts. *J. Climate*, **27**, 3169–3207, https://doi.org/10.1175/JCLI-D-13-00360.1.

Steinfeld, D., and S. Pfahl, 2019: The role of latent heating in atmospheric blocking dynamics: A global climatology. *Climate Dyn.*, **53**, 6159–6180, https://doi.org/10.1007/s00382-019-04919-6.

Takaya, K., and H. Nakamura, 2001: A formulation of a phase-independent wave-activity flux for stationary and migratory quasigeostrophic eddies on a zonally varying basic flow. *J.*

Atmos. Sci., **358**, 608–627, https://doi.org/10.1175/1520-0469(2001)058<0608:AFOAPI>2.0.CO;2.

Teng, H., G. Branstator, H. Wang, G. A. Meehl, and W. M. Washington, 2013: Probability of US heat waves affected by a subseasonal planetary wave pattern. *Nat. Geosci.*, **6**, 1056–1061, https://doi.org/10.1038/ngeo1988.

——, ——, A. B. Tawfik, and P. Callaghan, 2019: Circumglobal response to prescribed soil moisture over North America. *J. Climate*, **32**, 4525–4545, https://doi.org/10.1175/JCLI-D-18-0823.1.

Wilks, D. S., 2011: *Statistical Methods in the Atmospheric Sciences.* 3rd ed. International Geophysics Series, Vol. 100, Academic Press, 704 pp.

Yasui, S., and M. Watanabe, 2010: Forcing processes of the summertime circumglobal teleconnection pattern in a dry AGCM. *J. Climate*, **23**, 2093–2114, https://doi.org/10.1175/2009JCLI3323.1.

Yasunari, T., H. Nakamura, K.-M. Kim, N. Choi, M.-I. Lee, Y. Tachibana, and A. da Silva, 2021: Relationship between circum-Arctic atmospheric wave patterns and large-scale wildfires in boreal summer. *Environ. Res. Lett.*, **16**, 064009, https://doi.org/10.1088/1748-9326/abf7ef.

Yeh, S.-W., Y.-J. Won, J.-S. Hong, K.-J. Lee, M. Kwon, K.-H. Seo, and Y.-G. Ham, 2018: The record-breaking heat wave in 2016 over South Korea and its physical mechanism. *Mon. Wea. Rev.*, **146**, 1463–1474, https://doi.org/10.1175/MWR-D-17-0205.1.